50-275/323-OLA
6/17/87
I-SC-7

DOCUMENT 4
REF #21

Nuclear Engineering and Design 80 (1984) 315–329
North-Holland, Amsterdam

SEISMIC RESPONSE OF A FREE STANDING FUEL RACK CONSTRUCTION TO 3-D FLOOR MOTION

Alan I. SOLER

Professor of Mechanical Engineering and Applied Mechanics, University of Pennsylvania, Philadelphia, Pennsylvania, USA

Krishna P. SINGH

Vice President of Engineering, Joseph Oat Corporation, Camden, New Jersey, USA

Received January 1984

Seismic analysis of free standing submerged racks is complicated by the presence of water and structural non-linearities such as fuel assembly cell impact and floor interface friction. A direct time integration technique has been proposed to analyze this class of structures. Application of the time integration technique on a fourteen degree of freedom lumped mass model of the rack reveals some heretofore unpublished quirks in the structure's behavior. The method of analysis is utilized to compare the seismic response of some representative rack designs. Results show wide differences in the structural response, depending on the fabrication details of racks.

1. Introduction

Subsequent to the US government announcement of an indefinite suspension of spent fuel reprocessing in 1977, the nuclear power industry has scrambled to increase its capacity for on-site storage. The storage pools in most of the commercial reactors were initially designed to store $1\frac{1}{3}$ core worth of spent fuel. The storage rack modules, built for storing the spent fuel in the pool, were typically of open lattice construction. The racks were anchored to the pool floor, and were frequently braced to the side walls of the pool and to each other. Wide pitch (center-to-center spacing) between the storage locations ensured subcriticality of the fuel array. Ostensibly, the most viable and cost effective procedure to increase fuel pool storage capacity lay in replacing these rack modules with the so-called high density racks. The latest version of high density racks consists of cellular storage locations arranged in a tight pitch with neutron absorber materials interposed between the cells to maintain nuclear subcriticality. Matching of the new "high density rack supports" with the original floor anchor locations is usually quite cumbersome, if not impossible. Moreover, it is desirable to minimize the in-pool installation time for personnel radiation safety. These considerations, among others, prompted the evolution of the free standing high density racks storage concept. Increasingly, the new generation high density racks are being designed for free standing installation. The structural analysis of such racks under postulated floor motions, referred to as Safe Shutdown and Operating Basis earthquakes in the lexicon of the nuclear power industry, is the subject of this paper. Representative of other work in this area of interest is the rather qualitative paper by Habedank and co-authors [1].

A free standing rack module is a highly non-linear structure. During a seismic event the fuel assemblies can "rattle" inside their storage locations, and the module itself may slide on the pool floor. Furthermore, the rack may lift off at one or more support feet locations causing impact between pool floor and the rack support structure. Exigency of the market place calls for economies in design and construction; however, reduction in the rack structural strength can only be made after an exhaustive analysis of the resultant non-linear effects. In this paper we present a technique which can be utilized to make such an analysis.

To illustrate the procedure, we consider two types of rack construction; one in which the storage cells are attached to each other along their long edges in a certain pattern (honey-comb construction) and another

Sierra Club 7

NUCLEAR REGULATORY COMMISSION

Docket No. 50-275-OLA Official Exh. No. SC#7

In the matter of P G+E Company

Staff ______ IDENTIFIED ✓

Applicant ______ RECEIVED ______

Intervenor ✓ REJECTED ______

Cont'g Off'r ______

Contractor ______ DATE 6-17-87

Other ______ Witness ______

Reporter Harry Stunne

in which the connection between the cells is made only at the top and bottom (end connected tube construction). The latter construction involves only a fraction of the welding of the former, and therefore is a far more economical design. From a safety standpoint, the overriding concern relates to the increase in the rack stress levels and rigid body displacements as the inter-cell longitidutinal welds are eliminated. It is necessary to develop a methodology to address such concerns during the initial design and licensing effort. This paper is intended to provide such a tool.

A storage rack is a structure submerged in water which greatly complicates its motion. Proper simulation of rack dynamics requires consideration of hydraulic coupling and virtual mass effects. Such effects are included in this analysis using simplified models. Since our object herein is to establish a tool for comparison purposes only, we propose a fourteen degrees-of-freedom model to simulate rack behavior. A more comprehensive model has been employed by the authors in analyzing racks for individual plants [2]. It is important to emphasize that what we are demonstrating here is a simpler version of what would be required to qualify an actual unit; however, the methodology employed to develop the model is essentially the same.

Comparison of different rack geometries on the basis of their structural response is affected by three major variables; (i) the acceleration time history, which varies from plant to plant, (ii) the fraction of module storage locations occupied, (iii) and the limiting static and dynamic coefficients of friction at the rack and pool floor interface. In order to draw tenable conclusions, analyses are performed using three arbitrary sets of earthquake time histories. Two conditions of rack loading (all or half of the locations occupied), and two values of the coefficients of friction are also considered. In all a total of six cases are utilized to infer characteristics of the rack structural behavior.

The three orthogonal seismic excitations are applied coincidentally. The results reveal some striking peculiarities of the rack 3-D structural reponse. The marked increase in the rack stress levels and displacements predicted by this study as the design is varied from the "honey-comb" to "end connected" construction highlights the problem areas of the latter design. Perhaps more important, beyond the numerical results presented here, the analysis suggests a methodical technique to evaluate candidate designs for a particular application.

2. Theory

We consider a system governed by absolute generalized coordinates $p_i(t)$, $i = 1,2 \ldots N_z$. All internal forces contributing to system deformation are associated with generalized extensions $\delta_j(p_i)$. Internal force elements F_j may be non-linear functions of the generalized deformations $p_i(t)$ such as gap or friction elements. Lagrange's equations, written in terms of generalized forces $Q_i(t)$, and generalized external forces $G_i(t)$ are

$$\frac{\mathrm{d}}{\mathrm{d}t}\left(\frac{\partial T}{\partial \dot{p}_i}\right) - \frac{\partial T}{\partial p_i} = Q_i(t) + G_i(t) \; i = 1,2 \ldots N_z. \tag{1}$$

Since all of the $p_i(t)$ are independent, it is easily demonstrated that

$$Q_i(t) = \sum_{k=1}^{N_f} F_k \frac{\partial \dot{\delta}_k}{\partial \dot{p}_i} = \sum_{k=1}^{N_f} F_k B_{ik}, \tag{2}$$

where the dot $(\cdot)$ indicates time derivative and B_{ik} are called coupling coefficients [3]. B_{ik} relate the generalized velocities $\dot{p}_i(t)$ and the generalized extension rates $\dot{\delta}_K(t)$. The system kinetic energy T is written as

$$T = \frac{1}{2} \sum_{i=1}^{N_z} \sum_{j=1}^{N_z} M_{ij} \dot{p}_i \dot{p}_j. \tag{3}$$

For a geometrically linear system (equilibrium equations based on the undeformed configuration), the generalized masses M_{ij} are independent of coordinates p_k. Using eqs. (2) and (3) in eq. (1) yields the system equations of motion in the form

$$[M]\{\ddot{p}\} = [B]\{F\} + \{G\}, \tag{4}$$

where $[M]$ is of order $N_z \times N_z$; $[B]$, the coupling coefficients matrix, is of order $N_z \times N_f$, $\{p\}$, $\{G\}$ are column matrices containing N_z rows, and $\{F\}$ is a column matrix containing N_f rows. A set of inertially decoupled equations evolved from eq. (5), is

$$\{\ddot{p}\} = [M]^{-1}[B]\{F\} + [M]^{-1}\{G\} \tag{5}$$

Eq. (5) is solvable by direct integration techniques using a time history computer code described in ref. [3] (p. 336).

3. Fuel rack model

The following items should be considered in the development of any fuel rack–fuel assembly dynamic model:

3.1. Modelling of the rack structure

The rack structure may be modelled by elastic beam elements as long as appropriate cross section properties can be derived and as long as shear deformation and rotatory inertia effects are included. In specific design applications, the authors have used four beam elements and five nodal points to describe the rack structure. In this paper, since the emphasis is on a comparison of two different rack geometries, we have adopted a simpler model for the rack structure involving only a single beam element. This simplification helps to focus attention on the main differences between the two rack configurations studied; namely, the significant difference in the shear resistance.

3.2. Modelling of the fuel assemblies

Each fuel assembly should be treated as an individual distributed mass elastic element. In the actual fuel rack, an element may be located anywhere, in the $x-y$ plane and will impact with the fuel rack surrounding metal at one or more vertical locations. An assemblage of fuel assemblies will certainly not move in phase during a seismic event. For the purposes of evolving a conservative model, we have assumed that all of the fuel assemblies move as a unit; thus, the impacts with the fuel rack are magnified leading to higher stress and load levels. In a detailed model where the rack is simulated by five nodal points, impacts between fuel rack and fuel assemblies may occur at different levels; in the simpler model used herein for comparison purposes, we assume that impact between fuel rack and fuel assemblies occurs only at the top of the rack, and that 50% of the fuel assembly mass is involved in any impact with the rack. We emphasize that in any real design study, the possibility of impacts at various heights should be included in the model. For this illustrative comparison, we feel that the salient features of the behavior of each rack type will be correctly demonstrated with the simpler model.

Figs. 1 and 2 show the model considered in this paper. The fuel rack metal structure is a single beam element whose end points have a general six degree of freedom motion. The ensemble of fuel assemblies are conservatively assumed to move in phase under seismic excitation, and their effect on the fuel rack is considered to have the potential of 50% of the effective mass impacting the rack at the uppermost point. The offset of the lumped mass from the rack beam centerline enables simulation of a partially filled rack with induced torsional moments. The fuel rack base is a rigid plate,

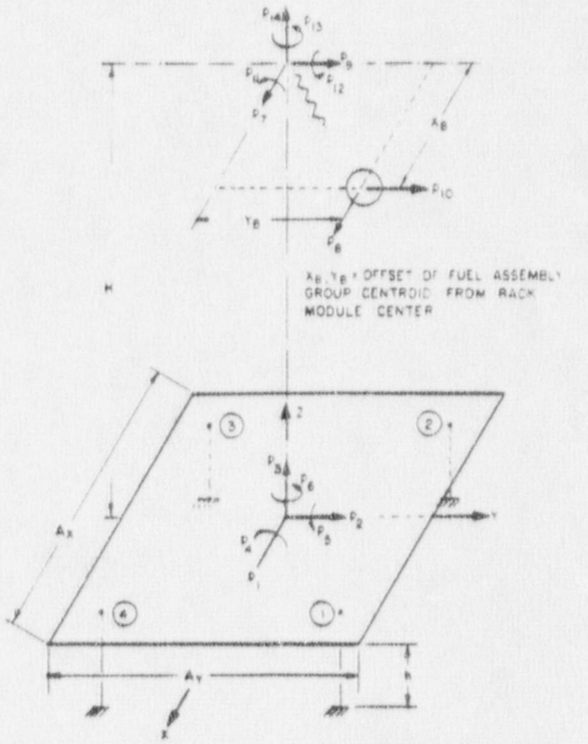

Fig. 1. Rack model showing degrees of freedom.

supported at the four corners by rigid supports that may slide or lift off the pool floor. The pool floor is excited by a known ground acceleration in three orthogonal directions.

Fluid coupling between rack cell walls and the ensemble of fuel assemblies is simulated by introducing appropriate inertial coupling terms into the system kinetic energy. Similar inertial coupling is introduced to

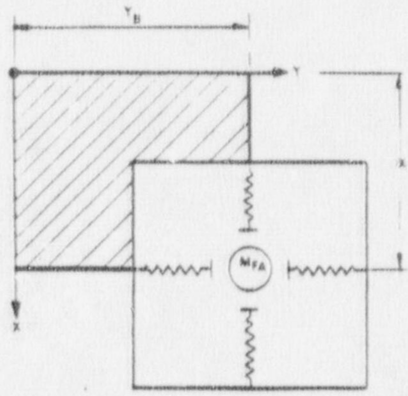

Fig. 2. Impact spring orientation at top of rack.

account for fluid structure effects between adjacent racks. Fluid damping effects are neglected in this study. As shown in fig. 2, potential impacts between the rack beam and the lumped mass representing the fuel assemblies are accounted for by inclusion of appropriate gap elements. The fluid inertial coupling terms are based on nominal clearances in this investigation; however, it has been shown [4] that inclusion of large deformation effects near the impact points may considerably affect the results. Herein, we do not include the effects of gap closure on [redacted] some [redacted]

In computing kinetic energy contributions from the rack, we use appropriate consistent mass matrices. Therefore, the contribution to the system kinetic energy due to the rack, T_1, is given by

$$2T_1 = \{\dot{p}_3, \dot{p}_{14}\}^{\mathrm{T}}[M_{\mathrm{E}}]\begin{Bmatrix}\dot{p}_3\\ \dot{p}_{14}\end{Bmatrix} + \{\dot{p}_6, \dot{p}_{13}\}^{\mathrm{T}}[M_{\mathrm{T}}]\begin{Bmatrix}\dot{p}_6\\ \dot{p}_{13}\end{Bmatrix}$$
$$+ \{\dot{p}_1, \dot{p}_7, \dot{p}_5, \dot{p}_{12}\}^{\mathrm{T}}[M_{\mathrm{B}}]\begin{Bmatrix}\dot{p}_1\\ \dot{p}_7\\ \dot{p}_5\\ \dot{p}_{12}\end{Bmatrix}$$
$$+ \{\dot{p}_2, \dot{p}_9, -\dot{p}_4, -\dot{p}_{11}\}^{\mathrm{T}}[M_{\mathrm{B}}]\begin{Bmatrix}\dot{p}_2\\ \dot{p}_9\\ -\dot{p}_4\\ -\dot{p}_{11}\end{Bmatrix}, \qquad (6)$$

where $[M_{\mathrm{E}}]$, $[M_{\mathrm{T}}]$ and $[M_{\mathrm{B}}]$ are the appropriate mass matrices for extensional, torsional and flexural motions. If A, I_{p} are the rack cross section effective metal area and polar moment of inertia, respectively, then

$$[M_{\mathrm{E}}] = \frac{\rho_c^* A H}{3}\begin{bmatrix}1 & \frac{1}{2}\\ \frac{1}{2} & 1\end{bmatrix};$$
$$[M_{\mathrm{T}}] = \frac{\rho^* I_p H}{3}\begin{bmatrix}1 & \frac{1}{2}\\ \frac{1}{2} & 1\end{bmatrix}, \qquad (7)$$
$$[M_{\mathrm{B}}] = \rho^* A H\begin{bmatrix}\frac{13}{35} & \frac{9}{70} & \frac{11H}{210} & -\frac{13H}{420}\\ \frac{9}{70} & \frac{13}{35} & \frac{13H}{420} & -\frac{11H}{210}\\ \frac{11H}{210} & \frac{13H}{420} & \frac{H^2}{105} & -\frac{H^2}{140}\\ \frac{-13H}{420} & \frac{-11H}{210} & \frac{-H^2}{140} & \frac{H^2}{105}\end{bmatrix} \qquad (8)$$

ρ^* and ρ_c^* are effective mass densities accounting for fluid effects. The contribution to the system kinetic energy due to the rack base is

$$2T_2 = m_{b_1}\dot{p}_1^2 + m_{b_2}\dot{p}_2^2 + m_{b_3}\dot{p}_3^2 + I_x\dot{p}_4^2 + I_y\dot{p}_5^2 + I_z\dot{p}_6^2, \qquad (9)$$

where m_{b_i}, I_x, I_y, I_z are the effective mass, and mass moments of inertia of the base, including fluid mass effects.

The contribution to system kinetic energy due to fluid coupling between fuel rack and fuel assemblies is expressed by the 2-D model given in ref. [5]. The necessity for accounting for 3-D fluid structure interaction is a question that merits future study. Using the 2-D approximation, we obtain for the kinetic energy due to rack–assembly interaction,

$$2T_3 = A_{22}(\dot{p}_7^2 + \dot{p}_9^2) + A_{11}(\dot{p}_8^2 + \dot{p}_{10}^2)$$
$$+ 2A_{12}(\dot{p}_7\dot{p}_8 + \dot{p}_9\dot{p}_{10}). \qquad (10)$$

Similarly, the kinetic energy due to fluid coupling between a fuel rack and adjacent structure is given as

$$2T_4 = B_{11}^{(x)}\dot{p}_1^2 + B_{11}^{(y)}\dot{p}_2^2 + B_{11}^{(x)}\dot{p}_7^2 + B_{11}^{(y)}\dot{p}_9^2$$
$$+ 2B_{12}^{(x)}\dot{p}_1\dot{U}_1 + 2B_{12}^{(y)}\dot{p}_2\dot{U}_2 + 2B_{12}^{(x)}\dot{p}_7\dot{U}_1$$
$$+ 2B_{12}^{(y)}\dot{p}_9\dot{U}_2 + O(\dot{U}_1^2, \dot{U}_2^2), \qquad (11)$$

where $U_i (i = 1, 2, 3)$ are specified pool floor seismic motions.

Finally, the contribution to the system kinetic energy due to the mass of the fuel assembly group is written as

$$2T_5 = \lambda M(\dot{p}_8^2 + \dot{p}_{10}^2) + M(\dot{p}_3 + Y_B\dot{p}_4 - X_B\dot{p}_5)^2$$
$$+ (1 - \lambda)M\left[(\dot{p}_1 - Y_B\dot{p}_6)^2 + (\dot{p}_2 + X_B\dot{p}_6)^2\right]. \qquad (12)$$

M is the total fuel assembly mass and λ is the mass fraction assumed acting at the top of the rack in the horizontal plane. We have assumed that vertical movement of the fuel assemblies is equal to the vertical movement of the rack base at fuel assembly centroid location, and that the fuel assembly mass fraction $(1 - \lambda)M$ moves with the base in the X–Y plane. In the study herein, we have arbitrarily set $\lambda = 0.5$ which implies that 50% of the fuel assembly mass is involved in the impact process and the impacts all occur at the top of the rack. If more conservatism is desired λ may be increased. It would be far better to include more degrees of freedom and allow for the possibility of impacts below the top level, however, than to attempt to determine a proper value for λ. For the purposes of the comparison simulation here, it is felt that the value of λ

used will not negate any conclusion developed as long as λ is sufficient to induce significant impacts between rack and assemblies. Eqs. (6)–(12) establish the system mass matrix $[M]$ in eq. (4) for the 14×14 model considered herein. We introduce displacement coordinates $q_i(t)$, relative to ground, defined as follows:

$$\begin{aligned} p_i &= q_i + U_1(t); & i &= 1,7,8, \\ p_i &= q_i + U_2(t); & i &= 2,9,10, \\ p_i &= q_i + U_3(t); & i &= 3,14, \\ p_i &= q_i; & i &= 4,5,6,11,12,13. \end{aligned} \tag{13}$$

The governing equations may be represented as follows:

$$\sum_{j=1}^{14} M_{ij} \ddot{q}_j = Q_i(t) + G_i(t) - [\alpha_{i1} \ddot{U}_1 + \alpha_{i2} \ddot{U}_2 + \alpha_{i3} \ddot{U}_3]$$

$$i = 1,2,\ldots,14. \tag{14}$$

In what follows, we discuss briefly the computation of some of contributions to the elements of the set of equations [14].

4. Fluid added mass effects

Consider a typical cell with an internal fuel assembly shown in fig. 3. Assuming that the assembly and the cell are vibrating, it is shown by Fritz [5] that the constant coefficients A_{ij} of eq. (10) are given as

$$A_{11} = M_H;\ A_{12} = -(M_1 + M_H);\ A_{22} = M_1 + M_H, \tag{15}$$

where M_1 = fluid mass displaced by fuel assembly, M_H = hydrodynamic mass. We use the Fritz model for concentric cylinders employing equivalent radii R_1, R_2 defined as

$$R_1 = a^*/\sqrt{\pi}, \quad R_2 = b^*/\sqrt{\pi}, \tag{16}$$

a^* is the side length of the square fuel assembly and $b^* > a^*$ is the inside dimension of a typical square cell; i.e. the nominal clearance between assembly and cell is $(b^* - a^*)/2$.

For a rack of height H, assuming all assemblies move in phase, we obtain

$$M_1 = \pi \rho_w H R_1^2 f_a, \tag{17}$$

where f_a is the number of cells containing spent fuel assemblies. If the nominal gap g is defined as $g = (b^* - a^*)/2$, then ref. [5] suggests that the hydrodynamic mass is

$$M_H = \frac{R_1}{g} M_1 / (1 + 12 R_2^2 / H^2). \tag{18}$$

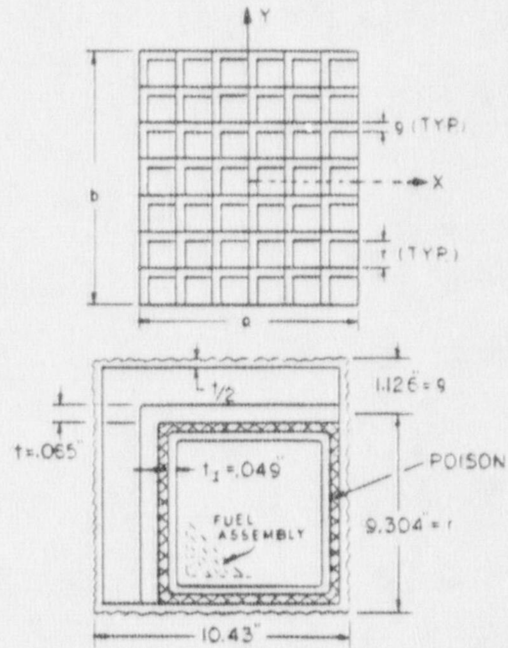

Fig. 3. Rack cross section and typical cell geometry – honeycomb construction.

The fluid mass that would fill the cell volume in the absence of the fuel assembly is denoted by M_2 in ref. [5]; the effect of this virtual fluid mass is incorporated directly in eq. (8) by defining an effective ρ^*.

The effect of fluid inside of the rack structure has been accounted for in the kinetic energy term $T_2(A_{ij})$. [redacted] now consider the effect of the fluid outside of the [redacted] We consider fig. 4 which shows a vibrating vertical wall of width W and height H. Following case 13 of ref. [5], we assume the hydrodynamic mass term as

$$M_H = \frac{\rho_w W^3 H}{12 g_0 \psi}; \quad \psi = 1 + \frac{W}{H}. \tag{19}$$

Then, in the fourteen degree of freedom simulation model, the coefficients, B_{11}, B_{12} at each level are given as

[redacted] (20)

with W being the value appropriate for X or Y motion.

The above discussion is concerned with fluid coupling effects induced by horizontal vibrations. To account for fluid effects in vertical vibrations, we simply define an effective mass density for the base plate using case 6 of ref. [5] and add it to the base plate metal mass.

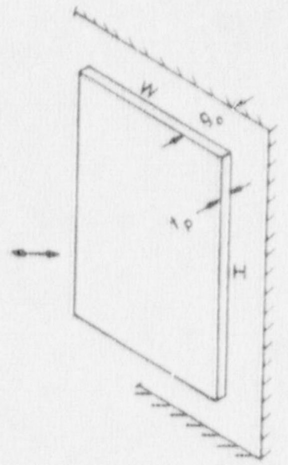

Fig. 4. Fuel rack wall model used to obtain flud coupling.

The total effective mass density is then used in the computation of m_{b_3}, I_x, I_y for the base plate. The effect of virtual fluid movements on the rack is simulated by defining an effective mass density ρ_v^* in the matrix $[M_E]$ in eq. (8). ρ_v^* is computed by adding to the rack metal mass, a mass equal to the mass of fluid displaced by the rack.

5. Internal forces

The internal force elements representing system elasticity, disappative friction and impact effects are simulated by using standard spring, friction and gap elements described in ref. [3]. The model shown in fig. 1 contains 6 elastic springs to model two bending planes, extension, and torsion of the rack beam. The model contains four gap elements modelling contact between the fuel assembly lumped mass and the top of the rack. The model used four gap elements alligned in the vertical direction and located at the x, y coordinates of the base plate supports to simulate the support behavior in the vertical direction and has sixteen friction elements to simulate support leg flexibility and the sliding potential of the supports. Finally, eight rotational frictional elements at the base supports are used to simulate resisting moments due to floor–structure interaction. Full details of the behavior of these elements and the development of their associated coupling coefficients are found in ref. [3]; herein, we simply specify the spring rates associated with each of the elements.

5.1. Rack elasticity (6 elements)

$$K_{\mathrm{TORSION}} = GIp/H,$$
$$K_{\mathrm{EXTENSION}} = EA/H,$$
$$K_{\mathrm{SHEAR}} = \frac{12EI}{H^3(1+\phi)}; \quad \phi = \frac{12EI\alpha}{GAH^2},$$
$$K_{\mathrm{BENDING}} = EI/H. \tag{21}$$

The coefficient α represents the effect of shear deformation, and I is the area moment of inertia of the cross section associated with beam bending. Note that one shear and bending spring pair is needed for each plane of bending.

5.2. Impact spring rate (4 gap elements)

The potential impact between fuel assembly mass and fuel rack is simulated by incorporation of a spring–gap combination. Each impact elements acts in compression only with spring constant given as

$$K_I = f_a 64\pi D/a^2; \quad D = Et^3/12(1-\nu^2). \tag{22}$$

K_I is determined by assuming that the impact is simulated by a uniform pressure acting over a circular section of cell wall of radius a and thickness t. The radius a is taken as $b^*/\sqrt{\pi}$ where b^* is the inside dimension of an individual cell and f_a is the number of cells containing fuel assemblies.

5.3. Support leg spring rate (4 gap elements)

The effect of support legs at each corner of the fuel rack base is simulated by four compression only gap elements to permit lift off of any or all supports. The local spring rate K_s for a support of height h is

$$\frac{1}{K_S} = \frac{1}{K_F} + \frac{1}{K_{LF}} + \frac{1}{K_{LR}}, \tag{23}$$

where $K_F = EA_S/h$; A_S = support leg cross section area, and

$$K_{LF} = 1.05E_c B/(1-\nu^2); \quad K_{LR} = 1.05\eta EB/(1-\nu^2). \tag{24}$$

K_{LF} represents the local elasticity of the pool floor with E_c being the Young's modulus of concrete and B being the width of the support leg pad [3]. K_{LR} represents the local elasticity of the rack just above the support leg; the coefficient η is taken arbitrarely as equal to the ratio of the metal area of single cell to included area of single cell.

5.4. Floor rotational and friction elements

The effect of local floor elasticity on rocking motion (support leg bending) is represented by rotational springs with spring rate ([3] p. 293).

$$K_H = E_c B^3/6(1-\nu^2). \tag{25}$$

These rotational springs are moment limited since if edging of the pad occurs, no further moment can be resisted.

Associated with each support leg compression element spring are two orthogonal friction elements located in the plane $Z = -h$ (see fig. 1). The friction element local spring rate is assumed as the spring constant of a support leg when considered as a guided cantilever beam of length h under an end load P. Therefore, from ref. [6], assuming that the support has area moment of inertia I_s when considered as a beam,

$$K_f = \frac{12EI_s}{h^3}\frac{1}{(1+\psi)}; \quad \psi = 8.52\frac{I_s}{A_s h^2} - 4.157\left(\frac{I_s}{A_s h^2}\right)^{3/2}. \tag{26}$$

6. Application to typical units

Figs. 3 and 5 show a cross section through a level of the rack structure of two practical rack constructions. The first is a fully connected honeycomb construction (HCC) which is considered as a beam-like structure with cross section dimensions b and a, having certain area and inertia properties; the second is an end connected tube construction (ETC) which has no shear transfer capability between tubes except at top and bottom of the rack. For the HCC rack, eq. (21) can be used directly to model rack elasticity since the entire cross section is capable of beam-like shear transfer; we need only examine the cross section details to derive expressions for A, I, I_p. For the ETC construction, however, since no shear transfer between cells can occur, we must undertake additional analysis in order to arrive at the proper spring rates for eq. (21).

Fig. 6 shows a free body of the rigid ring connecting all of the tube-like cells at $z = H$ and constrains them to move as a unit. If there are J cells at level i, then equilibrium requires that for a 2-D motion

$$M^* = \sum_{j=1}^{J}\left[\sum_i (M_{ij} + y_i N_{ij})\right],$$

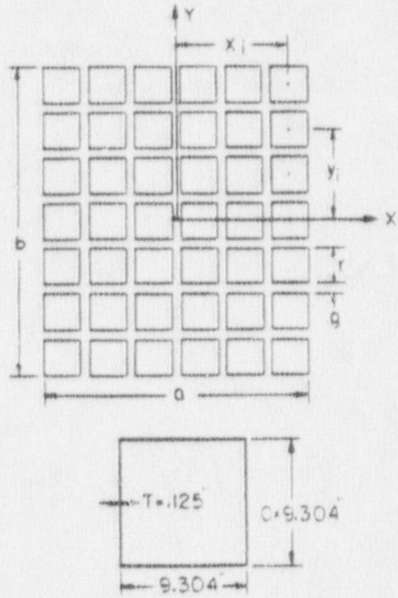

Fig. 5. Rack cross section and typical cell geometry, unconnected tube construction.

$$V^* = -\sum_{j=1}^{J}\left(\sum_i^I V_{ij}\right); \quad N^* = \sum_{j=1}^{J}\sum_i N_{ij}. \tag{27}$$

Castigliano's Theorem for the ith tube yields (assuming

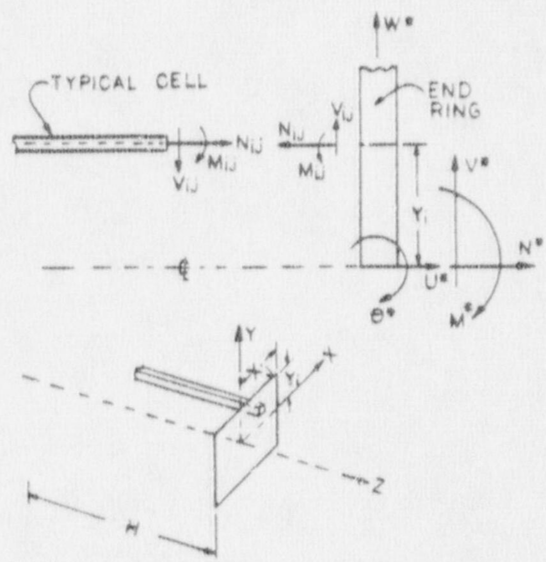

Fig. 6. Free body analysis of end ring in ETC rack.

a fixed base)

$$V_{ij} = -\frac{12EI}{H^3}W^* - \frac{6EI}{H^2}\theta^*,$$

$$M_{ij} = +\frac{6EI}{H^2}W^* + \frac{4EI}{H}\theta^*. \tag{28}$$

Also, bearing in mind the constraint of the end closure, we have,

$$N_{ij} = \frac{EA}{H}\left(U^* + y_i\theta^*\right). \tag{29}$$

In eqs. (28), (29), A, I refers to the properties of the individual cell, and we have neglected shear effects in the bending of the individual cells. Using eqs. (28), (29), in eq. (27) yields, for the case of n total cells in the unit,

$$M^* = +\frac{6E(nI)W^*}{H^2} + \frac{4E}{H}\left(nI + \sum_j\sum_i \frac{y_i^2A}{4}\right)\theta^*,$$

$$V^* = +\frac{12EnI}{H^3}W^* + \frac{6EnI}{H^2}\theta^*,$$

$$N^* = \frac{nEA}{H}U^*. \tag{30}$$

If we now replace eq. (30) by the corresponding equations for an equivalent uniform beam acted upon by end generalized forces M^*, V^*, N^*, and having effective cross section area A^*, inertia property I^*, and shear coefficient ϕ^*, we can show that the A^*, I^*, ϕ^* [for use in eq. (21)] which correspond to the ETC unit are given as

$$\frac{I^*}{1+\phi^*} = nI; \quad A^* = nA,$$

$$\frac{(4+\phi^*)I^*}{1+\phi} = 4\left(nI + \sum_{j=1}\sum_i \frac{y_i^2A}{4}\right), \tag{31}$$

so that

$$I^* = nI + \sum_j\sum_i y_i^2A; \quad \phi^* = \sum_i\sum_j y_i^2A/nI. \tag{32}$$

The results for A^*, I^*, ϕ^* can be used in eq. (21) in lieu of A, I, ϕ. It is clear that between the two geometries the only essential difference is in the magnitude of ϕ^*. The considerably larger value of ϕ^* obtained using eq. (32) for the ETC unit (as opposed to eq. (21) for the HCC unit) leads to a much smaller spring rate K_{SHEAR} being obtained for the ETC unit. It remains only to compute a value for I_p for both the HCC and the ETC configurations, and then to apply the simulation to typical in-service units.

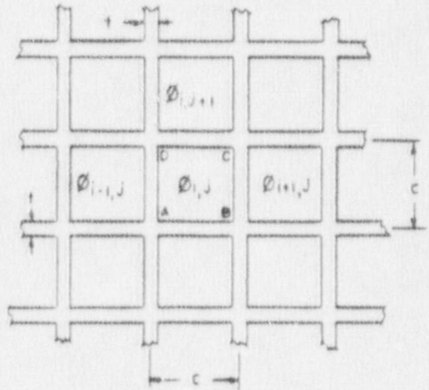

Fig. 7. HCC cross section for torsional rigidity analysis.

The torsional analysis for the HCC unit is based on the classical analysis of St Venant described in ref. [7] and applied to the cross section of fig. 7. By using the membrane analogy for the torsion problem, it can easily be shown that I_p for the HCC construction is simply ([7], p. 278)

$$I_p)_{HCC} = K_1(Gt/c)a^3b, \tag{33}$$

where K_1 is a tabulated function of b/a.

An analysis of the end cross section of the ETC construction using fig. 8, yields

$$I_p^* = I_p)_{ETC} = nI_p + \frac{24(1+\nu)}{H^2}I\sum\left(X_K^2 + Y_K^2\right). \tag{34}$$

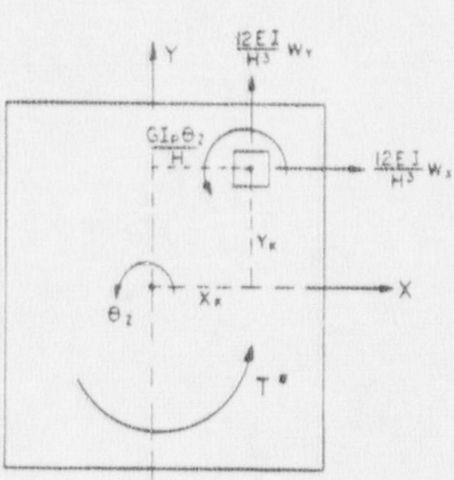

T* = TOTAL CROSS SECTION TORQUE
θ = ANGLE OF TWIST/UNIT LENGTH

Fig. 8. ETC end cross section under torsion.

where I_p, I are the area polar and bending inertia properties of an individual cell, and n is the total number of cells in the unit.

It should be emphasized that in the above analysis, we have assumed that the ends of the individual tubes are assumed to be connected in such a manner as to enforce the requirement that plane sections remain plane. This requirement may or may not be satisfied in any specific ETC design.

7. Application to typical configuration

We consider the configurations of figs. 3 and 5 for the case $b = 124.128''$ (315.3 cm), $a = 92.8125''$ (235.7 cm) having a 9×12 cell arrangement for a total of 108 cells. The support legs are assumed to be four $8'' \times 12'' \times 1''$ (20.4 cm × 30.5 cm × 2.54 cm) plate sections forming a box at each corner. Table 1 shows the spring rates computed for the two units assuming that the material is stainless steel having a Young's modulus $E = 28.3 \times 10^6$ psi (195 kPa) and the rack height $H = 161.125''$ (409.26 cm).

The seismic load–time histories used have statistically independent components in the global directions. The particular records used are those from three different plant specifications. (See figs. 9–11 showing one horizontal component.)

For the HCC unit, net beam forces and moments are used to compute extreme fiber stresses in the rack and in the supports on the basis of the formula

$$\sigma = \frac{|N|}{A} + \frac{|M_1|C_1}{I_1} + \frac{|M_2|C_2}{I_2}, \tag{35}$$

where A, I_1, I_2 are the appropriate geometric properties for the supports or for the entire rack cross section of the HCC unit. As noted previously, the use of the total cross section properties for rack stress evaluation is justified for the HCC unit since the full cross section is available for shear transfer. The evaluation of stress in the ETC unit requires some additional analysis. The cell whose centroid is at X_c, Y_c in the cross section experiences a direct stress of the form

$$\sigma_0 = \frac{E}{H}\left[(q_{14} - q_3) + Y_c(q_{11} - q_4) - X_c(q_{12} - q_5)\right]. \tag{36}$$

Due to bending of the cells in two planes, we have, for a cell of nominal cross section ($c \times c$), at the base of the rack

$$\frac{2\sigma_{BX}}{c} = -\frac{6E}{H^2}\left[(q_9 - q_2) + X_c(q_{13} - q_6)\right] - \frac{2E}{H}\left[q_{11} - q_4\right] - \frac{6E}{H} q_4, \tag{37}$$

$$\frac{2\sigma_{BY}}{c} = -\frac{6E}{H^2}\left[\quad - q_1) - Y_c(q_{13} - q_6)\right] + \frac{2E}{H}(q_{12} - q_5) + \frac{6E}{H} q_5. \tag{38}$$

The maximum rack stress in any cell wall can be constructed, at any time instant, from the expression

$$\sigma_{MAX} = |\sigma_0| + |\sigma_{BX}| + |\sigma_{BY}|. \tag{39}$$

We emphasize that eq. (39) does not include any local stress effects induced by non-rigidity of the rack base, load transfer between supports and adjacent cells or tubes, etc.

For a given time history of stress in the supports, in the HCC rack cross section, or in the ETC individual cell cross section, a determination of unit structural integrity may be carried out. In accordance with ref. [8], structural integrity may be interpreted as setting limits on forces and moments acting separately or together on a defined cross section. For the HCC construction, the entire rack cross section can be used in the structural integrity evaluation; for the ETC construction, we must examine the cross section of the critical cell.

In addition to stress limitations, adjacent racks must not impact during a seismic event. In the simulation herein, virtual mass effects from gaps between racks a

Table 1
Spring rates for model

Item	HCC	UTC
Area of cell	4.379 sq. in	4.652 sq. in
I_{Cell}	= 35.55 in^4	33.56 in^4
I_x^* (unit)	616 926 in^4	654 996 in^4
I_y^* (unit)	346 825 in^4	367 993 in^4
Area of unit	472.9 in^2	502.4 in^2
I_p^o (unit)	111 321.8 in^4	14 939 in^4
$\phi_{y,x};\phi^*_{y,x}$	2.35;1.322	179.71;100.53
$K_{TORSION}$ [eq. (21)]	7.520×10^9 in #/rad	1.009×10^9 in #/rad
$K_{EXTENSION}$	0.8306×10^8 #/in	0.8818×10^8 #/in
$K_{SHEAR-Y}$	0.1214×10^8 #/in	0.294×10^6 #/in
$K_{SHEAR-X}$	0.1214×10^8 #/in	0.294×10^6 #/in
K_{BX}	0.1084×10^{12} in #/rad	0.1150×10^{12} in #/rad
K_{BY}	0.0609×10^{12} in #/rad	0.0646×10^{12} in #/rad
K_{IMPACT} (fa = 108)	0.715×10^6 #/in	5.084×10^6 #/in
K_S [eq. (23)]	0.0925×10^8 #/in	0.0958×10^8 #/in
K_H [eq. (25)]	5.971×10^8 in #/rad	5.971×10^8 in #/rad
K_f [eq. (26)]	2.004×10^8 #/in	2.004×10^8 #/in

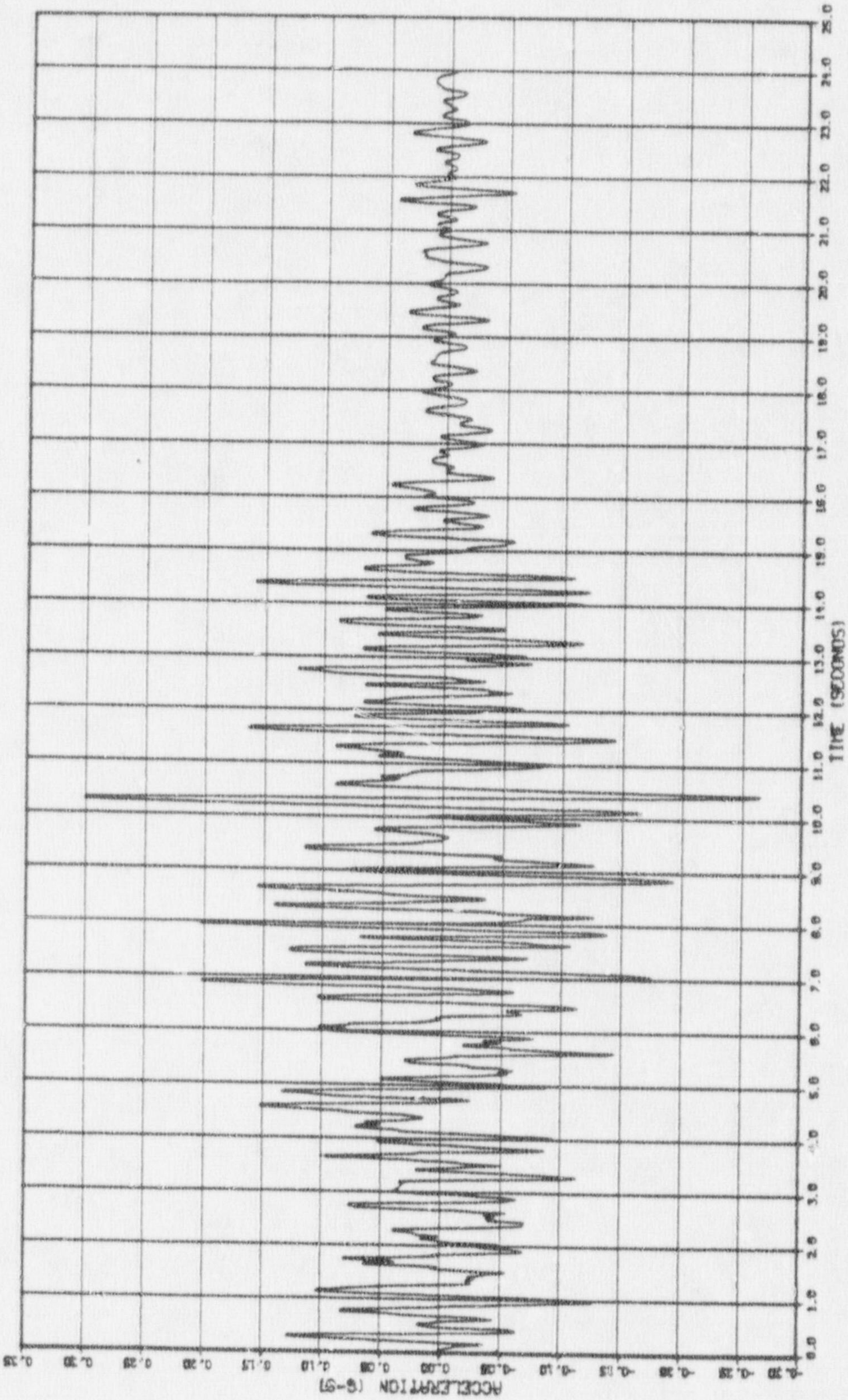

Fig. 9. Earthquake 1.

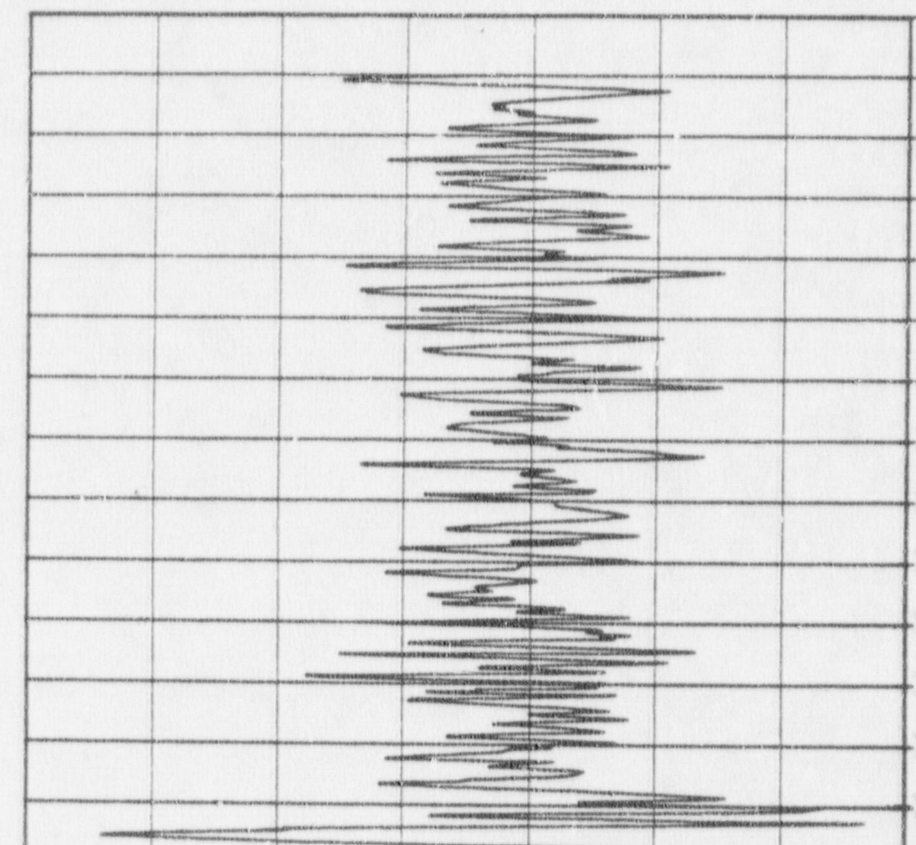

Fig. 10. Earthquake 2

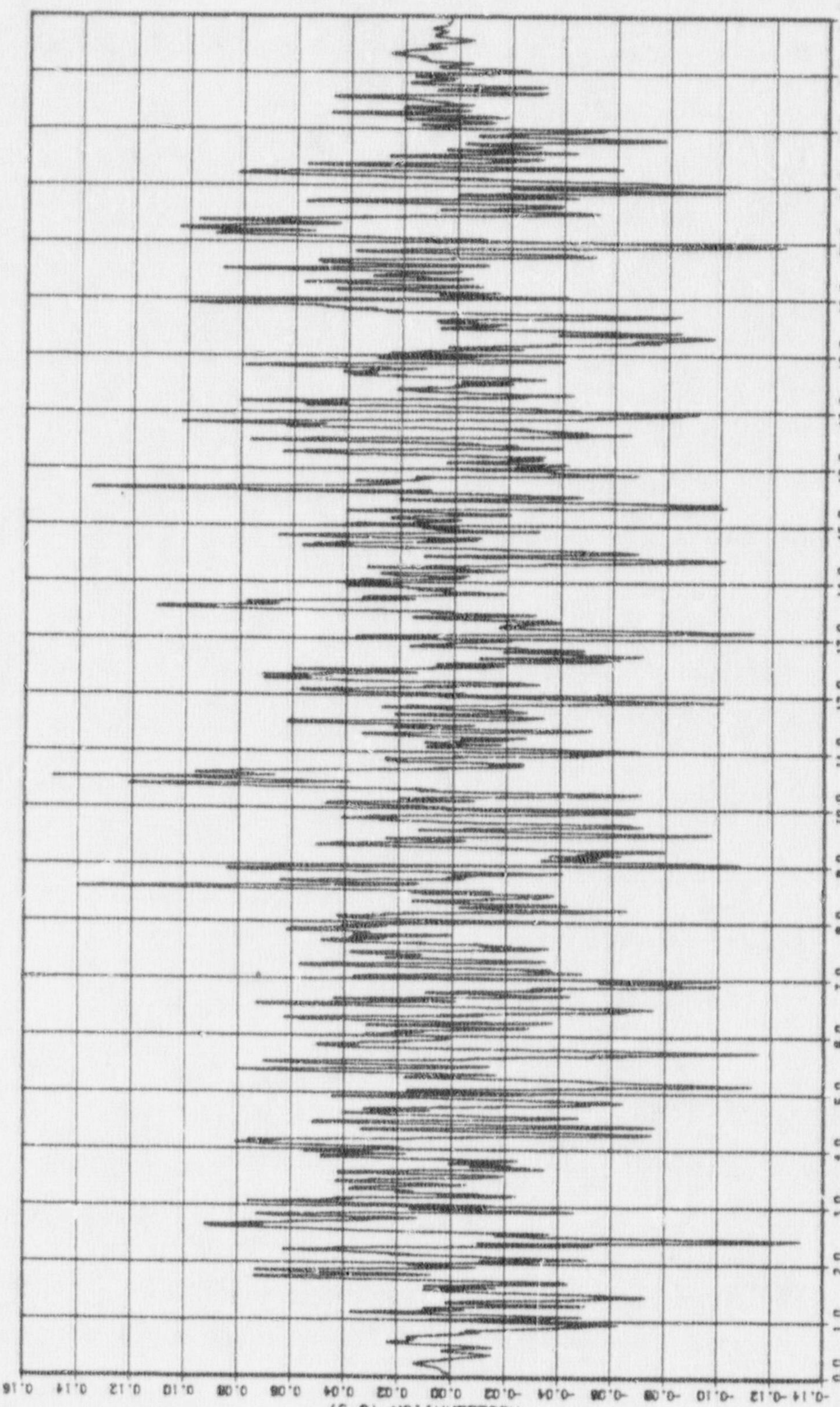

Fig. 1. Earthquake 3.

Table 2
Simulation studies

Case	Description	Seismic load
1	full rack; COF = 0.8	fig. 9 (0.302 × 1.5 = max. g. level) 15 s duration
2	full rack; COF = 0.2	fig. 9 (0.302 × 1.5 = max. g. level) 15 s. duration
3	full rack; COF = 0.8	fig. 10 (0.17 × 1.5 = max. g. level) 12 s. duration
4	full rack; COF = 0.8	fig. 11 (0.15 × 1.5 = max. g. level) 20 s. duration
5	half rack load; COF = 0.8	same as case 1
6	full rack; COF = 0.8	fig. 10 (0.17 × 2.5 = max g. level) 12 s. duration

have been included based on adjacent rack spacing equal to 3" (76.2 mm). Therefore, assuming the worst motion of adjacent racks, inter-rack impact is precluded if the maximum corner deflection of the rack in either direction is less than 50% of the rack spacing.

To assess the two rack constructions, the simulations given in table 2 are performed. Values used for coefficients of friction, $0.2 < COF < 0.8$ are accepted upper and lower bound values. Simulations 1–5 are performed with the seismic input amplified by 1.5 on all three input directions. Simulation 6 is performed with the appropriate seismic inputs amplified by 2.5. Thus, case 6, when compared to case 3 shows the effect of employing different amplifications on the same seismic event. Simulation 5, using a half loaded rack, highlights the effect of rigid body rotation of the rack around the vertical axis. The half loaded cases assume that all cells on one side of the unit diagonal are loaded. In all cases, structural damping of 2% is assumed at a frequency of 20 Hz. Table 3 summarizes the results obtained for stresses and table 4 shows the maximum corner displacements and maximum floor loads transmitted by the rack. We may define factors R_i which are limited to the value 1 or 2 for an OBE, or SSE event, respectively [8].

Table 3

CASE	Honeycomb construction				End connected tube construction			
	Rack		Support		Rack		Support	
	R1	R4,R5	R1	R4,R5	R1	R4,R5	R1	R4,R5
1	0.002	0.081	0.385	1.46	0.200	1.21	0.613	1.898
2	0.001	0.038	0.182	0.356	0.104	0.642	0.232	0.548
3	0.001	0.068	0.322	0.964	0.155	0.955	0.372	1.27
4	0.001	0.065	0.319	0.957	0.180	1.12	0.406	1.35
5	0.003	0.127	0.485	1.93	0.123	1.004	0.294	1.082
6	0.002	0.061	0.513	1.664	0.204	1.322	0.499	1.50

Table 4
Maximum rack deflections/transmitted loads

Case	Honeycomb construction					End connected tube construction				
	X (in)	Y (in)	Max. [a)] flr. ld. (lbs)	Single leg ld. (lbs)	Impact load (lbs)	X (in)	Y (in)	Max. [a] flr. ld. (lbs)	Single leg ld. (lbs)	Impact load (lbs)
1	1.175	0.084	536 600	257 700	201 400	1.049	1.629	1 280 000	411 300	578 500
2	0.573	0.489	232 600	121 000	138 300	1.624	1.55	345 700	156 100	241 800
3	0.187	0.086	402 200	215 900	49 370	0.499	0.753	809 400	257 700	357 800
4	0.111	0.064	334 800	211 600	113 100	0.624	0.568	772 700	297 700	350 500
5	1.35	1.62	496 300	340 900	79 540	2.145	2.392	602 200	200 000	181 500
6	0.826	0.343	611 000	309 800	216 800	0.856	1.45	985 500	343 100	588 300

[a)] Static load = 184 000# for Cases 1,2,3,4,6,
= 103 300# for Case 5.

R_1 = direct stress on a net section/allowable OBE tensile (compressive stress),
R_2 = gross shear on a net section/allowable OBE shear,
R_3 = maximum bending stress in one plane/allowable OBE value,
R_4 = combined flexure and compression ratio,
R_5 = additional combined flexure and tension (compression) ratio.

It has been found from a large number of simulations of different HCC racks that factors R_4 or R_5 usually govern structural integrity in both rack and in support legs. In table 3, we show only values for R_1, and R_4 or R_5 at the most critical location.

8. Discussion and conclusions

From the simulation results, we can draw the following conclusions:

(1) An accurate picture of the results can only be obtained using 3-D nonlinear time history analysis regardless of the rack modelled. A large contribution to the maximum rack horizontal displacements can be made during an instant when the rack is only supported on one foot and the seismic loads cause a pivot of the rack about the only remaining contact point.

(2) Maximum displacements, with a full rack, may be found when the upper bound coefficient of friction value is used. This can be explained by noting that there is a greater tendency for an individual support leg to stick when in ground contact and therefore the possibility of pivoting during an instant when a single foot is in contact is increased.

(3) For the seismic events considered here, stress levels in the supports legs have the same order of magnitude in both HCC and ETC racks.

(4) Stress levels in the rack cells, above the base, are significantly higher in the ETC unit than in the HCC unit. The ratio of cell stress levels (ETC/HCC) is 10 to 20 in the simulations considered here. While the levels reported here due to beam type stress resultants may not imply violation of gross failure criteria, it is noted that effects near the supports, and construction details not modelled herein, will certainly induce stress raisers on the computed levels reported here. For example, any flexibility at the rack base plate will cause more load to be shifted to the outermost cells; also, local stress raisers will certainly be imposed on those cells nearest the supports. Therefore, it is prudent to ensure that the rack stress levels in the thin walls of the cells, induced by gross dynamic motions, remain low enough so that stress raisers have minimal effect on unit performance. By the very nature of the construction, stress raisers should tend to be higher in the ETC rack compared to what might be present in the HCC rack; therefore, gross stress levels (prior to inclusion of stress raisers) in the thin walled cells on the order of the allowable stress should be viewed with concern.

(5) Because of its increased tendency to slide, the ETC rack generally experiences greater horizontal displacements. For some of the simulations studied herein, inter-rack impact may occur since the predicted maximum displacements exceed fifty per cent of the assumed spacing between adjacent racks.

(6) The maximum load (static plus dynamic impact) transmitted to the floor from the total number of support feet in contact at any instant is larger with the ETC rack. This is attributed to the increased propensity of the ETC rack to lift off the pool floor, possibly pivot on a single support leg, and subsequently re-contact the floor with a substantial impact.

(7) The increased displacements found for the case of the half loaded rack dramatically show the effect of 3-D motions and the potential for rigid body rotations about the vertical axis. It is noted that this effect is substantially affected by the initial assumption on the amount of fuel assembly mass participating in impacts with the cell walls.

On the basis of the above results, we conclude that in general, the HCC rack offers greater safety margins in the rack body, is less prone to excessive displacement, and results in lower dynamic loading on the pool floor. Although the model used herein is relatively simple, it does exhibit the features of the 3-D motion and the expected impacts. In any real design application a more elaborate model would be called for, which accounts for impacts at different levels, additional [illegible] degrees of freedom, etc.. In the study reported on here, however, the simplest model is appropriate since we week only a comparison of results from two different constructions.

The numerical studies presented in the foregoing point up the significance of inter-cell welding. The longitudinal welds connecting the cells in the honeycomb construction are found to improve the stress levels and kinematic response of the rack significantly over the end connected construction. The difference is certain to be all the more important if consolidated pin storage is contemplated.

Nomenclature

T	system kinetic energy
Q_i, G_i	generalized internal, external forces
p_i, q_i	generalized coordinates
N_f, N_z	number of internal force elements, degrees of freedom
$[B]$	coupling coefficient matrix
$[M_E]$,$[M_B]$;$[M_T]$	mass matrices for extension; bending; and torsion of rack
ρ^*, ρ_i^*	effective mass densities
A; H	rack cross section metal area; rack height
m_{bi}, I_x, I_y, I_z	mass and inertia properties of rack base
$U_i(t)$	specified seismic motion of pool floor
M	total mass of fuel assembly
$B_{ij}^{(x)}, B_{ij}^{(y)}, A_{ij}$	fluid coupling coefficients [eqs. (10) and (11)]
λ	defined in eq. (12)
M_H	hydrodynamic mass [eq. (18)]
f_c	number of cells in fuel rack
f_a	number of cells containing fuel assemblies
h	height of rack support leg
A_s, I_s	metal area, metal inertia of support leg cross section
I^*, A^*, ϕ^*, I_p^*	equivalent rack properties for ETC unit
c	side length of a single fuel cell
t	wall thickness of fuel cell
$R_i (i = 1,2\ldots5)$	structural integrity factors
E	Young's Modulus of rack metal
X_c, Y_c	centroid of fuel assemblies moving us a group

References

[1] G. Habedank, L.M. Habip and H. Swelim, Dynamic analysis of storage racks for spent fuel assemblies, Nucl. Engrg Des. 54 (1979) 379–383.

[2] Spent fuel pool modification for increased storage capacity, Quad Cities Units 1&2, Commonwealth Edison Company N.R.C. Document No. 50-264, 50-265 (June, 1981).

[3] S. Levy, and J.P.D. Wilkinson, The Component Element Method in Dynamics (McGraw-Hill, New York, 1976).

[4] A.I. Soler and K.P. Singh, Dynamic coupling in a closely spaced two body system vibrating in a liquid medium: the case of fuel racks, 3rd Keswick Int. Conf. Vibration in Nuclear Plants, May 1982, Keswick, United Kingdom.

[5] R.J. Fritz, The effect of liquids on the dynamic motions of immersed solids, ASME J. Engrg. Industry (February, 1972) 167–173.

[6] S.P. Timoshenko, Strength of Materials, Vol. 1, 3rd Ed. (McGraw-Hill, New York) p. 175.

[7] S.P. Timoshenko and J. Goodier, Theory of Elasticity, 3rd ed. (McGraw-Hill, New York, 1951) pp. 258–315.

[8] ASME Code, Section III, Subsection NF, and Appendix XVII (1980).

UNITED STATES
NUCLEAR REGULATORY COMMISSION
WASHINGTON, D. C. 20555

May 26, 1987

MEMORANDUM FOR: John Milligan
Technassociates

FROM: Emile L. Julian, Acting Chief
Docketing and Service Branch

SUBJECT: DIABLO, EXHIBITS

Any documents filed on the open record in the Braidwood proceeding and made a part of the official hearing record as an exhibit is considered exempt from the provisions of the United States Copyright Act, unless it was originally filed under seal with the court expressly because of copyright concerns.

All of the documents sent to TI for processing fall within the exempt classification.